Monthly Notices
of the
ROYAL ASTRONOMICAL SOCIETY

MNRAS **448,** 207–220 (2015) doi:10.1093/mnras/stu2732

Runaway stars as cosmic ray injectors inside molecular clouds

M.V. del Valle,[1,2]★ G. E. Romero[1,2] and R. Santos-Lima[3]

[1]*Instituto Argentino de Radioastronomía, C.C.5, 1894, Villa Elisa, Buenos Aires, Argentina*
[2]*Facultad de Ciencias Astronómicas y Geofísicas, Universidad Nacional de La Plata, Paseo del Bosque, 1900 La Plata, Argentina*
[3]*Instituto de Astronomia, Geofísica e Ciências Atmosféricas, Universidade de São Paulo, São Paulo, SP 05508-090, Brazil*

Accepted 2014 December 19. Received 2014 December 19; in original form 2014 May 14

ABSTRACT

Giant molecular clouds (GMCs) are a new population of gamma-ray sources, being the target of cosmic rays (CRs) – locally accelerated or not. These clouds host very young stellar clusters where massive star formation takes place. Eventually, some of the stars are ejected from the clusters, becoming runaway stars. These stars move supersonically through the cloud and develop bowshocks where particles can be accelerated up to relativistic energies. As a result, the bowshocks present non-thermal emission, and inject relativistic protons in the cloud. These protons diffuse in the GMC interacting with the matter. We present a model for the non-thermal radiation generated by protons and secondary pairs accelerated in the bowshocks of massive runaway stars within young GMCs. We solve the transport equation for primary protons and secondary pairs as the stars move through the cloud. We present non-thermal emissivity maps in radio and in gamma-rays as a function of time. We obtain X-ray luminosities of the order of $\sim 10^{32}$ erg s^{-1} and gamma-ray luminosities $\sim 10^{34}$ erg s^{-1}. We conclude that, under some assumptions, relativistic protons from massive runaway stars interacting with matter in GMCs give rise to extended non-thermal sources.

Key words: radiation mechanisms: non-thermal – ISM: clouds – cosmic rays – gamma-rays: ISM.

1 INTRODUCTION

Molecular clouds (MCs) are good targets for Galactic cosmic rays (CRs) since they are extended regions with great amounts of mass. These systems contain particle accelerators such as supernova remnants (SNRs), OB massive stars and pulsars. The relativistic particles accelerated in these sources add to the galactic CR population that illuminates the clouds producing gamma-rays (e.g. Casse, Montmerle & Paul 1981; Aharonian & Atoyan 1996; Torres, Dame & Digel 2005).

Giant molecular clouds (GMCs) are a new class of extended gamma-ray sources (e.g. Ackermann et al. 2012b; Fernandez et al. 2013). However, their potential as passive gamma-ray sources have been claimed since the beginning of gamma-ray astronomy and their emission was predicted in theoretical models long time ago (e.g. Kraushaar et al. 1972; Aharonian 1991; Combi & Romero 1995; Hunter et al. 1997). Not only passive, GMCs emit gamma-rays; recently the smaller and gas-rich star-forming regions Chamaeleon, R Coronae Australis, Cepheus and Polaris have been detected by *Fermi* (Ackermann et al. 2012a).

GMCs harbour young stellar clusters where massive stars form. Many stars with masses $M > 8$ M$_\odot$ might be ejected from the clusters (e.g. Perets & Šubr 2012), becoming runaway stars travelling through the cloud. Runaway stars have spatial velocities >30 km s^{-1} (e.g. Gies & Bolton 1986). Two mechanisms have been proposed for the origin of the high velocities in these stars. In the binary-supernova scenario one of the stars in a binary system is expelled during the supernova explosion of its companion (Blaauw 1961). In the other scenario, the dynamical-ejection model, the star is expelled through close gravitational interactions between members of a cluster or association (Leonard & Duncan 1988). Currently, the latter process is believed to be the most frequent (Fujii & Portegies Zwart 2011), but both mechanisms surely operate (Hoogerwerf, de Bruijne & de Zeeuw 2000).

The supersonic interaction between the wind of fugitive stars with the interstellar medium (ISM) produces a bowshock (e.g. van Buren & McCray 1988; Peri et al. 2012). The wind-swept material, gas, and dust are heated by the shock and radiated away in the infrared (IR) band (e.g. van Buren & McCray 1988; Kobulnicky, Gilbert & Kiminki 2010).

Both observational (Benaglia et al. 2010; López-Santiago et al. 2012; del Valle, Romero & De Becker 2013) and theoretical research (del Valle & Romero 2012, 2014) support the idea that bowshocks from massive runaway stars accelerate particles up to relativistic energies. Electrons lose their energy in the acceleration region, while protons escape, convected away by the shocked wind without losing much of their energy. The escaped protons then diffuse in the MC.

We propose here that protons accelerated in bowshocks from massive runaway stars embedded in MCs contribute to the cloud's CR population that produces the observed gamma-rays in these

★ E-mail: maria@iar-conicet.gov.ar

systems. The relativistic protons interact with the MC matter via p−p inelastic collisions (Aharonian & Atoyan 1996; Bosch-Ramon, Aharonian & Paredes 2005).

The favourite sources for accelerating particles in the ISM are SNRs, which can inject particles with total energies up to 10^{50} erg; it is believed that these sources are responsible for the bulk of the galactic CRs (Ginzburg & Syrovatskii 1964; Hillas 2005). MCs near SNRs produce gamma emission (e.g. Combi, Romero & Benaglia 1998). Three H.E.S.S. sources are firmly associated with an MC–SNR system. However, in the star-forming regions immersed in GMCs, besides SNRs, there exist very energetic sources such as young stars with powerful winds. A very massive star during its life (1–10 Myr) can inject into the ISM an amount of kinetic energy from its wind comparable to the SNR values. However, a young cluster has not lived enough time for an SNR to develop and to be able to inject relativistic particles into the cloud. Here, we proposed that runaway massive stars[1] could contribute to the local density of relativistic particles inside MCs, and produce significant non-thermal emission. An instrument with both good enough sensitivity and angular resolution, such as the forthcoming Cherenkov Telescope Array (CTA; see Actis et al. 2011),[2] can detect the produced emission and its expected morphology, that we estimate in this work.

We organized this article as follows. In Section 2, we briefly introduce MCs and their gamma-ray emission. Section 3 deals with runaway stars in MCs. There, we present the scenario adopted in this work. In Section 4, we describe the model and in Section 5, we describe the numerical method we use in the calculations. The results are given in Section 6. Finally, in Section 7, we discuss the results and offer our conclusions.

2 MOLECULAR CLOUDS

MCs are dense and cold regions that constitute the most dense component of the ISM. They have temperatures of the order of 10–20 K, and average densities of the order of 10^2 cm^{-3}. In these systems most of the new stars of the Galaxy are formed. Young stars are associated with the densest regions of the clouds ($n > 10^4$ cm^{-3}). In these cores of GMCs (with total masses between 10^3 and 10^6 M$_\odot$), the most massive stars are born.

In the Galaxy, the molecular gas is typically concentrated in big complexes or segments of spiral arms with sizes of the order of ∼1 kpc and masses of 10^7 M$_\odot$. These systems can contain many GMCs with sizes of ∼100 pc and masses of ∼10^6 M$_\odot$. These GMCs also contain substructures such as the cores with sizes of the order of ∼0.1 pc. In our Galaxy smaller clouds also exist with masses of ∼500 M$_\odot$ (e.g. Larson 2003).

The clouds have structure and turbulence at all scales. The gas density in these objects varies many orders of magnitude, the densest regions having densities as high as ∼10^5 cm^{-3}. The density profile is not well known, with different substructures present in the clouds (filaments, clumps, cores, etc.). Usually, the following profile is adopted for the density (e.g. Gabici, Aharonian & Blasi 2007):

$$n(R) = \frac{n_0}{1 + \left(\frac{R}{R_\mathrm{n}}\right)^\beta}, \quad (1)$$

where R is the distance from the cloud centre and R_n is the core radius. The index β is a free parameter.

MCs are magnetized, the magnetic field being important in their evolution and dynamics. The magnetic field is closely related to the gas density (Crutcher 1999), and it is described by the following profile:

$$B \sim 100 \left(\frac{n}{10^4\ \mathrm{cm}^{-3}}\right)^\eta\ \mu\mathrm{G}. \quad (2)$$

Here, $\eta = 0.5$. Although the correlation given in equation (2) between the gas density and the magnetic field has been found for the cores of MCs with densities greater than 10^3 cm^{-3}, it provides reasonable values for regions of lower density and it is usually extrapolated to the whole range of densities (e.g. Gabici et al. 2007; Pedaletti et al. 2013), although this correlation can be substantially reduced by turbulence (Santos-Lima et al. 2010).

The average age of MCs is ∼10 Myr (e.g. Bodenheimer 2011). The clouds are eventually destroyed and disrupted by ionization, outflows, and winds produced by the young stars.

2.1 Gamma-rays from MCs

As mentioned above, some GMCs are gamma-ray sources. Studies of the gamma-ray emission of nearby MCs (at distances ∼1 kpc) dated since the *COS-B* days (e.g. Bloemen et al. 1984; Hunter et al. 1994). Theoretical works on the CR illumination of nearby sources are even older (e.g. Black & Fazio 1973; Montmerle 1979). Diffuse gamma-ray emission has been detected from the galactic centre region, being spatially correlated with a GMC complex (Aharonian et al. 2006); star formation regions inside MCs also have been detected: Monoceros R2 (Martí et al. 2013), Westerlund 2 (Reimer et al. 2008), Westerlund 1 (Ohm, Hinton & White 2013), the region of Cygnus (Aharonian et al. 2005), and the Orion region, which includes three dense young star clusters (Hartmann 2009). Additionally, *Fermi* has been detecting nearby clouds (at distances $d < 300$ pc) in the energy range 250 MeV–10 GeV; these clouds have masses between 10^3 and 10^4 M$_\odot$ (Ackermann et al. 2012a). The gamma-ray luminosities observed in MCs vary between ∼10^{33} and 10^{35} erg s^{-1}.

Gamma-ray emission is of special interest because, when it is detectable, its study provides a good tool for investigating acceleration and propagation of CRs in the Galaxy (e.g. Aharonian 2001). MCs embedded in the galactic CR *sea* are expected to emit gamma-rays as passive sources. If particles can freely penetrate the clouds, the gamma-ray spectrum is expected to mimic the CR spectrum and the total gamma-ray luminosity depends only on the total mass of the cloud (e.g. Gabici 2011). However, CR penetration on MCs is a subject of debate. In general, the penetration might depend on the diffusion coefficient, a key parameter very hard to estimate both theoretically and observationally.

3 RUNAWAY STARS IN MCS

Numerical simulations and theoretical predictions indicate that many massive stars can be ejected with high velocities from their formation clusters by gravitational encounters. Runaway stars then move through their parental MC. The probability to eject a star

[1] No evidence exists so far of a strong shock or of non-thermal emission from the bowshock of a low-velocity (non-binary) massive star. A strong shock might not form due to the catastrophic adiabatic wind losses (Voelk & Forman 1982). In a runaway star, the stagnation point is much closer to the star.

[2] However, *Fermi*, in target mode, might have sufficient sensitivity to detect the emission.

from a massive cluster with velocity $V_\star$ is a power law $\propto V_\star^{-\nu}$, where $\nu = 3/2$ for slow runaways, and $8/3$ for fast ones (Perets & Šubr 2012). Additionally, the ejection probability increases with mass. *N*-body simulations show that during its life a cluster can eject ∼six stars with masses >8 $M_\odot$, independently of the cluster mass (Fujii & Portegies Zwart 2011). Observational evidence consistent with these results is found, for example, in the R136 cluster: six massive runaway stars are associated with it (Gvaramadze, Kroupa & Pflamm-Altenburg 2010; Bestenlehner et al. 2011).

Stellar bowshocks inside MCs might not be detectable in the IR because the emission produced by the whole cloud overshines individual contributions. Nevertheless, the presence of bowshocks can be inferred through the study of certain spectral lines and masers. Masers are collisionally excited by hydrogen which is heated by shock waves (e.g. Elitzur 1976).

A runaway star moving through an inhomogeneous medium produces variable non-thermal emission (del Valle & Romero 2014). The electrons yield the bulk of the non-thermal radiation, while most of the accelerated protons escape without losing much of their energy and then diffuse in the environment. Gamma-ray emission and secondary electron–positron pairs are produced through p−p interactions with matter. These pairs also diffuse in the cloud and produce non-thermal radiation by synchrotron process. The injected power in protons by the bowshock is a fraction of the kinetic power of the wind:

$$L_\mathrm{T} \sim \frac{1}{2}\dot{M}_\mathrm{w} V_\mathrm{w}^2, \tag{3}$$

where $\dot{M}_\mathrm{w}$ is the wind mass-loss rate and V_w^2 is the wind terminal velocity.

Here, we consider as a first approach a spherical young MC[3] of radius $R_\mathrm{MC} = 50$ pc and core radius $R_\mathrm{n} = 0.5$ pc. This cloud hosts a massive young stellar cluster. The density profile of the cloud is given by equation (1), with $\beta = 1$ (*boxy cloud*) and $n_0 = 10^4$ cm^{-3}. The total mass of the cloud is $M_\mathrm{MC} \sim 10^6$ $M_\odot$. We assume that the cluster ejects six massive stars in the last Myr. Additionally, we adopt in our simulations that all stars have been ejected at approximately the same time in random spatial directions, as illustrated in Fig. 1.

The ejection probability of a star is $\propto V_\star^{-\nu}$; therefore, it is more likely to eject stars of low velocity. We consider then three stars with velocity $V_\star \sim 30\,\mathrm{km\,s^{-1}}$, two stars of velocity $V_\star \sim 65\,\mathrm{km\,s^{-1}}$, and one of $V_\star \sim 100\,\mathrm{km\,s^{-1}}$. Also, runaway stars of spectral types O9 are more common than O4-type stars; then we consider one star of type O4I, three of type O9I, and two intermediate cases; the maximum energies we estimate for locally accelerated protons are 10^{14}, 10^{12}, and 10^{13} eV, respectively.[4] These parameters are shown in Table 1. The stars inject protons continuously during 1 Myr. The maximum energies that protons reach do not depend on the medium density (see del Valle & Romero 2014) and neither does the injected power, so these quantities are constant during the motion of the stars through the cloud.

[3] MCs can be disrupted by the action of the winds and radiation of the new stars. Evolved MCs are not expected to be spherical but annular; such a system will be considered elsewhere.

[4] These values are consistent with the maximum energies for protons obtained in del Valle & Romero (2014).

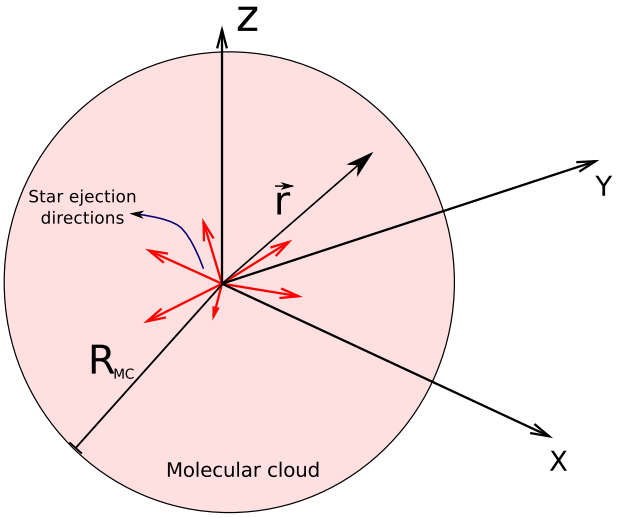

Figure 1. Random ejection directions of the six runaway stars ejected at the centre of a spherical MC (not to scale).

4 PHYSICAL MODEL

As mentioned, we do not take into account the physical details of the injectors (the stellar bowshocks); we consider them as punctual, moving with constant velocity $V_\star$ through the cloud, without perturbing the density distribution. The relativistic protons diffuse into the cloud. Because of the linear nature of the problem, we solve the equations for each star and sum all contributions to obtain the final result.

The spectral energy distribution N_p of the protons follows the transport equation:

$$\frac{\partial N_\mathrm{p}(\boldsymbol{r}, E, t)}{\partial t} = \nabla\cdot[D(\boldsymbol{r}, E)\nabla N_\mathrm{p}(\boldsymbol{r}, E, t)] - \frac{\partial}{\partial E}(P(\boldsymbol{r}, E)\, N_\mathrm{p}(\boldsymbol{r}, E, t)) + Q_\mathrm{p}(\boldsymbol{r}, E, t), \tag{4}$$

where $D(\boldsymbol{r}, E)$ is the diffusion coefficient of the particles, $P(\boldsymbol{r}, E) \equiv -(\mathrm{d}E/\mathrm{d}t)$ is the radiative energy loss rate, and $Q_\mathrm{p}(\boldsymbol{r}, E, t)$ is the injection function. We adopt a scalar diffusion coefficient[5] that depends only on the particle energy $D(\boldsymbol{r}, E) \equiv D(E)$; given the geometry of the scenario considered here, we adopt a spherical coordinate system (R, θ, ϕ), with its origin at the cloud centre (see Fig. 1). During the calculation for each star (see the details in Section 5), we adopt a coordinate system in which the star moves along the polar axis. Thus, the proton density function N_p depends spatially only on R and θ, i.e. $N_\mathrm{p} \equiv N_\mathrm{p}(R, \theta, E, t)$. In this coordinate system equation (4) becomes

$$\frac{\partial N_\mathrm{p}}{\partial t} = D(E)\left[\frac{1}{R^2}\frac{\partial}{\partial R}\left(R^2\frac{\partial N_\mathrm{p}}{\partial R}\right) + \frac{1}{R^2\sin\theta}\frac{\partial}{\partial\theta}\left(\sin\theta\frac{\partial}{\partial\theta}\right)\right] - \frac{\partial}{\partial E}(P(R, \theta, E)\, N_\mathrm{p}) + Q_\mathrm{p}(R, \theta, E, t). \tag{5}$$

The dominant losses for protons are p−p inelastic collisions, while the ionization losses are negligible in the range of energies considered (Aharonian & Atoyan 1996). The loss term is $P(R, \theta, E) = E\,(n(R)\,c\,\kappa_\mathrm{pp}\sigma_\mathrm{pp})$, where κ_pp is the inelasticity (∼0.45) and σ_pp is the cross-section for inelastic collisions. The dependence on

[5] In its more general form, the diffusion coefficient is a tensor (e.g. Berezinskii et al. 1990).

Table 1. Wind velocity and mass-loss rate, stellar velocity, injected power, proton maximum energies, and crossing time ($\tau = R_{MC}/V_\star$) for each runaway star considered (see the text).

$\star$ #	$V_\star$ (km s^{-1})	$\dot{M}_w$ (M$_\odot$ yr^{-1})	V_w (km s^{-1})	Power (erg s^{-1})	Max. energy (TeV)	τ (Myr)
1	30	10^{-4}	2200	3×10^{35}	100	1.6
2	30	10^{-6}	800	4×10^{32}	1	1.6
3	30	10^{-5}	1000	7×10^{33}	10	1.6
4	65	10^{-5}	1000	7×10^{33}	10	0.7
5	65	10^{-6}	800	4×10^{32}	1	0.7
6	100	10^{-6}	800	4×10^{32}	1	0.5

R and θ of the radiative losses is given through the density – see equation (1).

The σ_{pp} cross-section can be approximated by (Kelner, Aharonian & Bugayov 2006)

$$\sigma_{pp} = (34.3 + 1.88L + 0.25L^2)\left[1 - \left(\frac{E_{th}}{E_p}\right)^4\right]^2 \text{m}b, \quad (6)$$

where $L = \ln(E_p/1\text{TeV})$ and $E_{th} = 1.22$ GeV.

The injection function Q_p is

$$Q_p(R, \theta, E, t) = N_0\, E^{-2}\, \delta^3(\boldsymbol{r} - \boldsymbol{r}_\star), \quad (7)$$

where $\boldsymbol{r}_\star = \boldsymbol{V}_\star t$ is the position of each star with respect to the cloud centre; N_0 is the normalization constant which depends on the injected power in relativistic particles for each star, as discussed above. We only consider proton injection when the stars are inside the cloud (i.e. $t \leq \tau$).

The spectral energy distribution (SED) of secondary pairs $N_{e^\pm}$ obeys the same transport equation as protons (equation 5), but the radiative term $P(R, \theta, E)$ and the injection function $Q_{e^\pm}(R, \theta, E, t)$ are different. The pairs are injected through the decay of charged pions produced in the p−p collisions (e.g. Orellana et al. 2007). The injection of leptons can be calculated from (Kelner et al. 2006)

$$Q_{e^\pm}(R, \theta, E, t) = \int_{E_{e^\pm}}^{\infty} \sigma_{pp}(E_p)\, n(R)\, c\, N_p(R, \theta, E_p, t) \times F(E_{e^\pm}, E_p)\, \frac{dE_p}{E_p}, \quad (8)$$

where $F(E_{e^\pm}, E_p)$ is the electron spectrum of the decay $\pi \rightarrow \mu + \nu_\mu$.

The relevant losses for pairs are synchrotron radiation and relativistic Bremsstrahlung (see for example, Aharonian 2004, and references therein).

4.1 Diffusion

The diffusion coefficient is a key parameter in the study of the diffusion of energetic particles. It is a poorly determined quantity, from both the observational and theoretical point of view. The theoretical determination of the diffusion coefficient is a very complex task (e.g. Yan & Lazarian 2004, 2008) and observations are necessary to constraint the models. CR diffusion is a non-linear process in which the CRs generate the instabilities that produce the turbulence they interact with (e.g. Nava & Gabici 2013, and references therein). Near the particle accelerators, where the population of CRs is very high, the diffusion coefficient can significantly decrease through instabilities (Ptuskin, Zirakashvili & Plesser 2008; Yan & Lazarian 2011; Malkov et al. 2013). Furthermore, slow diffusion is expected in dense regions (e.g. Ormes, Ozel & Morris 1988).

Through gamma-ray observations of the SNR W28 – a remnant on its radiative phase, localized in a region of dense molecular gas – illuminating an MC, a significant suppression of the diffusion coefficient with respect to the averaged galactic values was reported (e.g. Gabici 2011). Also, Yan, Lazarian & Schlickeiser (2012) using a self-consistent model for the acceleration of CRs and the gamma-ray production in W28, required a high suppression of the ISM diffusion coefficient to match the gamma observations. In these studies, isotropic diffusion was considered. If the isotropic assumption is dropped, the conclusions are different. Under some physical conditions diffusion becomes anisotropic, particles diffuse preferentially parallel to the magnetic field lines (e.g. Casse, Lemoine & Pelletier 2002). An anisotropic treatment was developed in Nava & Gabici (2013), where the diffusion coefficient is not suppressed to fit the observations. Both scenarios fit the observations of the SNR W28, showing that a great uncertainty exists on the diffusion coefficient.

Here, we adopt a phenomenological approach similar to the one used in Gabici et al. (2007). The diffusion coefficient is a power law in the particle energy:

$$D(E) = \chi\, D_{10} \left(\frac{E}{10\,\text{GeV}}\right)^{\delta}, \quad (9)$$

where D_{10} is the value of D at $E = 10$ GeV. The power δ varies between 0.3 and 0.6 depending on the power-law spectrum of the turbulence of the magnetic field. The parameter $\chi < 1$ takes into account the suppression of the diffusion coefficient inside the turbulent medium of the cloud. For δ and D_{10}, we take values considered as typical in the Galaxy 0.5, and 10^{27} cm^2 s^{-1}, respectively (Berezinskii et al. 1990). We study two cases of χ: 10^{-1} – expected in dense regions – and 10^{-3} – an extreme case. As we are considering an isotropic diffusion coefficient, no specification of the magnetic field direction is required in our calculations.

4.2 CR sea

In order to compare the contribution of the injected protons with the CR background of the Galaxy, we calculate the CR flux expected in the cloud, following Gabici et al. (2007). CRs do not freely penetrate the cloud; they diffuse slowly, especially in dense regions. To get the CR distributions N_p^{CR} consistently with the parameters adopted, we solve the transport equation in steady state. This means, equation (5) with $\partial/\partial t = 0$, null injection function and the condition that the distribution N_p^{CR} at the edges of the cloud match the CR sea distribution. We consider only protons because it is the dominant CR component. We also consider the secondary pairs that the high-energy protons produce in their collisions with the cold protons. We

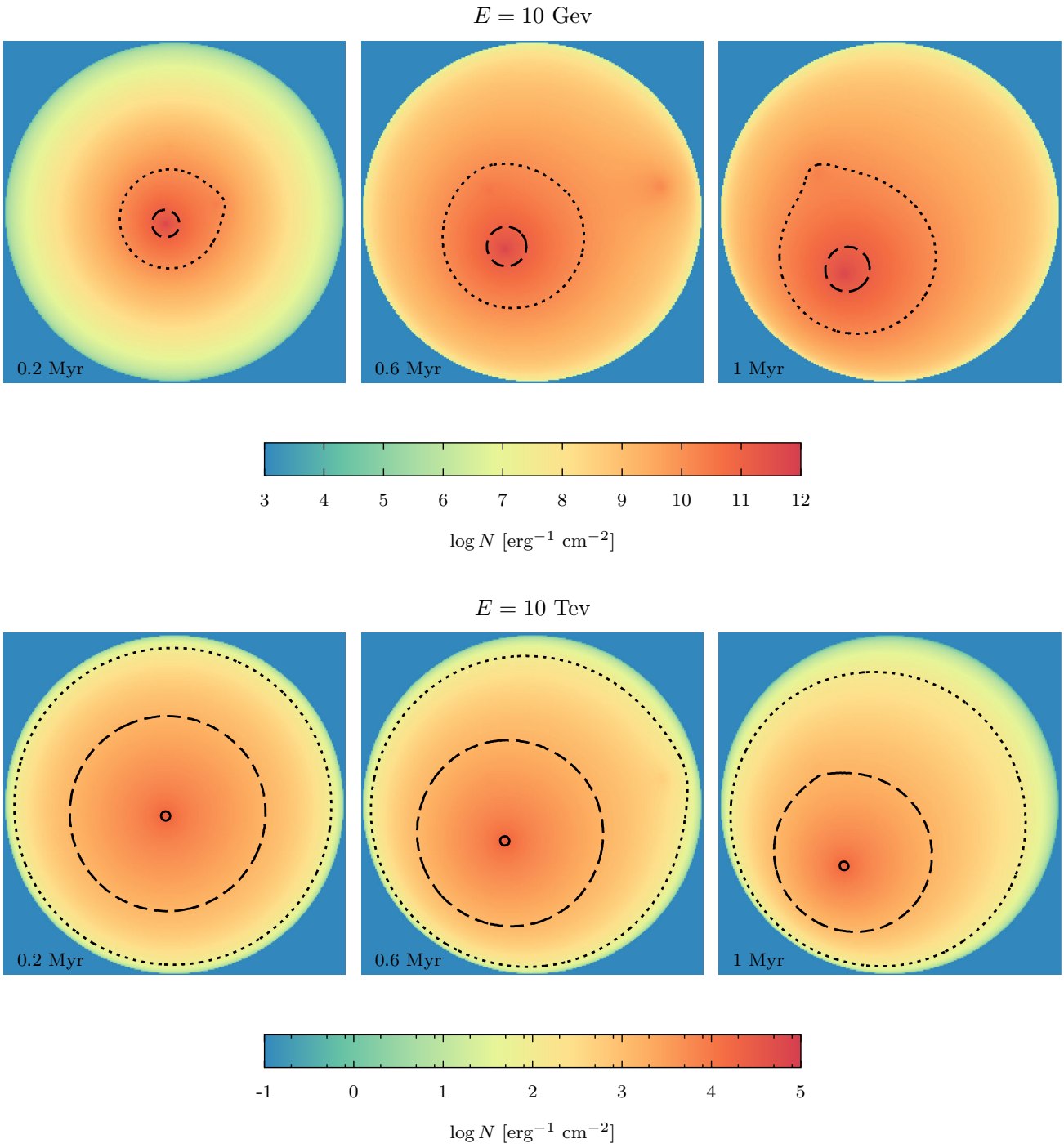

Figure 2. Proton distribution at fixed energy projected along the line of sight for the case $\chi = 10^{-1}$. Top: $E_p = 10$ GeV; bottom: $E_p = 10$ TeV. Time evolves from left to right. The level curves correspond to 0.1 (dotted), 1 (dashed), and 10 (continuous) times the CR background distribution.

take the galactic CR-flux equal to the locally observed one[6] (e.g. Simpson 1983):

$$J_{\rm CR}^{\rm gal}(E) = 2.2 \left(\frac{E}{\rm GeV}\right)^{-2.75} \ {\rm cm}^{-2}\,{\rm s}^{-1}\,{\rm sr}^{-1}\,{\rm GeV}^{-1}. \quad (10)$$

We also consider the case in which the background CR flux is one order of magnitude less than the locally observed flux, given by the latter equation.

[6] However, this assumption is ad hoc, see the discussion in Section 7.

4.3 Emission

We calculate the p−p emissivity for protons and the synchrotron emission produced by the secondary pairs. In the ISM, the luminosity produced by inverse Compton scattering is in general negligible compared to the p−p contribution (see Bosch-Ramon et al. 2005). Relativistic Bremsstrahlung is significant only at energies smaller than 1 GeV (Aharonian 2004; Gabici et al. 2007) and here we neglect it. In what follows we describe the numerical methods used.

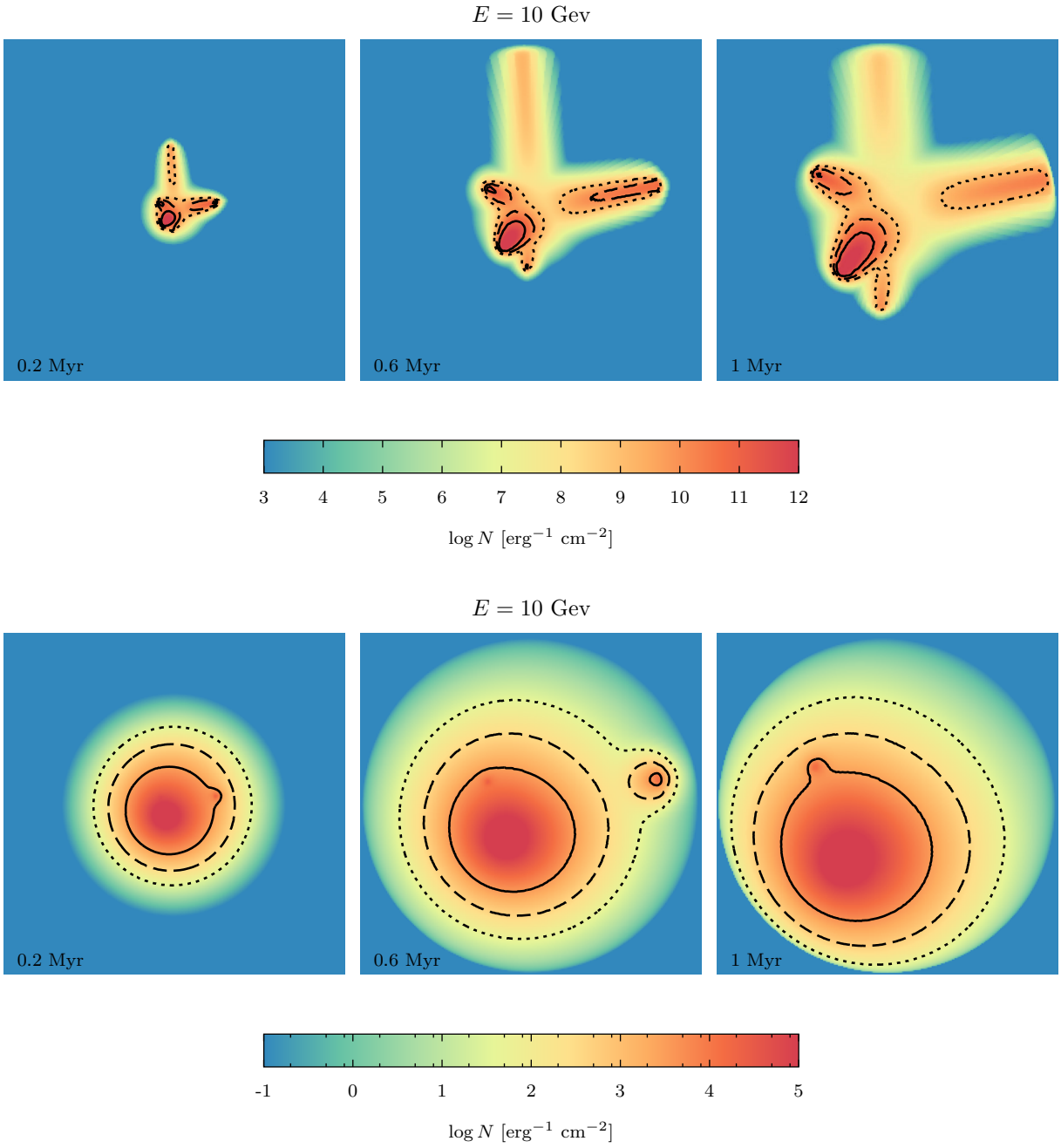

Figure 3. Same as the last figure, for $\chi = 10^{-3}$.

5 NUMERICAL METHODS

The transport equation is solved for a single CR injector at a time. We consider the star moving along the polar axis of an spherical system of coordinates. In this way, the system has azimuthal symmetry, allowing a reduction of the dimensionality of the problem. The coordinates of the particle distributions resulting from each injector star are then rotated (by randomly chosen angles, shown in Fig. 1) and interpolated into a 3D spatial grid. In this way, the resulting distribution of particles is obtained by summing the contribution coming from each star. Below, we describe the numerical methods employed for solving the problem for one injector.

We evolve the transport equations for protons and pairs simultaneously (throughout this section N represents the distribution of protons or pairs, without distinction) in a discrete grid of the phase space $(E, R, \theta) \in [1\,\mathrm{MeV}, 100\,\mathrm{TeV}] \times [0, 50\,\mathrm{pc}] \times [0, \pi]$, using the finite-volumes method. The phase space is therefore divided in a grid of cells with central values E_l, R_i, θ_j ($1 \le l \le L$, $1 \le i \le M$, and $1 \le j \le K$). The lengths of the cells (E_l, R_i, θ_j) are given by $\Delta E_l = E_{l+1/2} - E_{l-1/2}$, $\Delta R_i = R_{i+1/2} - R_{i-1/2}$, $\Delta\theta_j = \theta_{j+1/2} - \theta_{j-1/2}$, where $\alpha \pm 1/2$ ($\alpha = l, i, j$) are the values at the left/right interface of the cell. The energy grid (E_l, $1 \le l \le L$) is logarithmically spaced, while the radial (R_i, $1 \le i \le M$) and polar (θ_j, $1 \le j \le K$) grids are uniformly spaced. In the simulations presented

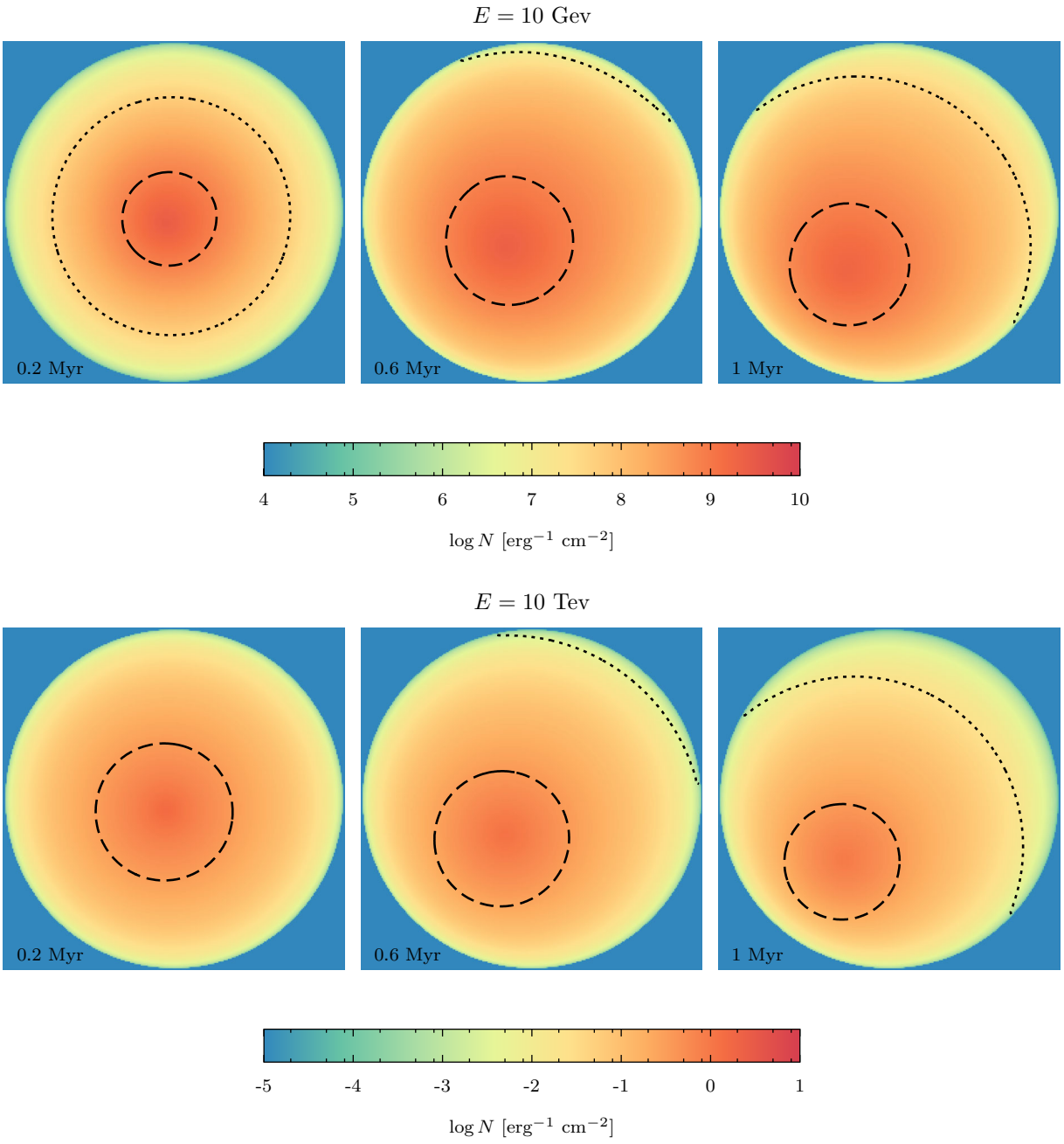

Figure 4. Distribution of $e^{\pm}$ pairs at fixed energy projected along the line of sight for the case $\chi = 10^{-1}$. Top: $E_e = 10$ GeV; bottom: $E_e = 10$ TeV. Time evolves from left to right. The level curves correspond to 0.1 (dotted), and 1 (dashed) times the pairs' background distribution.

in this work, we employ the grid resolution $(L, M, K) = (128, 64, 64)$.[7]

The density of particles at a given time t is represented inside each cell by the average value $N_{l,i,j}(t) \equiv N(E_l, R_i, \theta_j, t)$, i.e. the number of particles inside the discrete volume of the phase space $\Delta E_l \Delta R \Delta\theta$ at a time t is given by $N_{l,i,j}(t)\Delta E_l \Delta V_{i,j}$, where $\Delta V_{i,j} \approx 2\pi R_i^2 \Delta R \sin\theta_j \Delta\theta$.

At $t = 0$ we consider $N_{l,j,k}(t = 0) = 0$ for protons and pairs (i.e. no particles).[8]

The energy boundary conditions we impose to N are

$$N(E < 1 \text{ MeV}, R, \theta, t) = N(E > 100 \text{ TeV}, R, \theta, t) = 0, \qquad (11)$$

i.e. no particles outside the energy bounds. In fact, these limits do not influence the system evolution, because the upper limit is above the maximum energy of the injected protons, at the same time that

[7] When solving the distribution of particles for the galactic CR background, we extend the energy range to [1 MeV, 10^3 TeV]. Because of radial symmetry, the grid resolution employed is $(L, M, K) = (144, 64, 1)$.

[8] In order to obtain numerically the steady state solution for the distribution of the background CRs, we consider $N_{\mathrm{CR}\,l,j,k}(t = 0) = 0$ inside the MC, and we evolve the transport equation during enough time for the solution to become time independent.

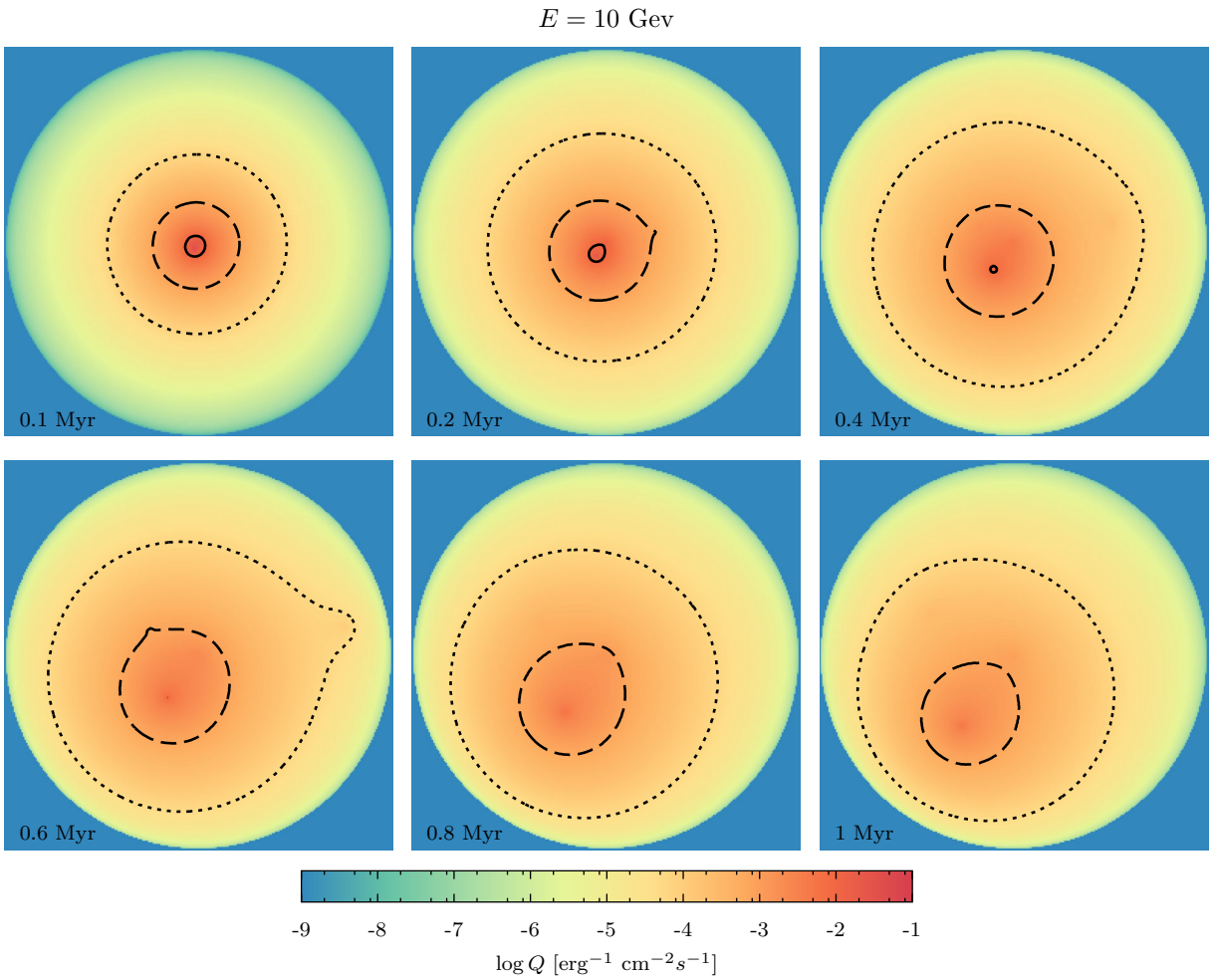

Figure 5. Gamma-ray emissivity evolution, projected along the line of sight for $\chi = 10^{-1}$. The photon energy is $E = 10$ GeV. Time evolves from top left to bottom right. The level curves represent 0.1 (dotted), 1 (dashed), and 10 (continuous) times the background emissivity.

the advection in the energy space is always directed to smaller energies. The lower bound is physically fixed because relativistic particles have kinetic energies greater or of the order of their rest mass. The spatial boundary conditions are

$$N(E, R > 50 \text{ pc}, \theta, t) = 0, \tag{12}$$

i.e. no particles outside the MC, and

$$\frac{\partial N(E, R, \theta = 0, t)}{\partial \theta} = \frac{\partial N(E, R, \theta = \pi, t)}{\partial \theta} = 0, \tag{13}$$

due to the azimuthal symmetry.

For the calculation of the CR background distribution (see Section 4.2) the following boundary conditions are used instead:

$$N_{\rm CR}(E > 10^3 \text{ TeV}, R, \theta, t) = 0, \tag{14}$$

and

$$N_{\rm CR}(E, R > 50 \text{ pc}, \theta, t) = \frac{4\pi}{c} J_{\rm CR} \left(\frac{E}{1 \text{ GeV}} \right)^{-\alpha}, \tag{15}$$

where the last condition is valid only for protons, and $J_{\rm CR}$ is the CR flux at $E = 1$ GeV. The other boundary conditions are identical to the ones described before. Here, we should remark that the upper boundary in the energy space affects the solution because, differently from the protons injected from the stars, there is no established cut-off at the CR highest energies. We keep the energy range broader enough to minimize these effects.

The numerical integration of the transport equation is performed using the operator splitting method, in the way described below. Each time-step integration evolves the particle density distribution on the grid $N^n_{l,i,j} \equiv N_{l,i,j}(t^n)$ from time t^n to time $t^{n+1} = t^n + \Delta t$, through three sub-steps described below.

First, we integrate only the losses term of the transport equation,

$$\frac{\partial N(E, R, \theta, t)}{\partial t} = -\frac{\partial}{\partial E} \left[F(E, N(E, R, \theta, t)) \right], \tag{16}$$

where the flux $F(E, N(E, R, \theta, t)) \equiv P(E) N(E, R, \theta, t)$ is an advection in the energy space. In the finite-volume formulation, we employed an upwind scheme of second order[9] for calculating the fluxes at the interface of the cells. The intermediate solution $N^{n+1/3}_{l,i,j}$ is then obtained from the solution $N^n_{l,i,j}$ at time t^n through the explicit Euler method:

$$\frac{N^{n+1/3}_{l,i,j} - N^n_{l,i,j}}{\Delta t} = -\frac{1}{\Delta E_l} \left(F^n_{l+1/2,i,j} - F^n_{l-1/2,i,j} \right). \tag{17}$$

Here, $F^n_{l\pm1/2,i,j}$ represents the numerical fluxes at the cell interfaces.

[9] We use the Piecewise Linear Method (PLM) with the Monotonic Central limiter, which is second-order accurate on a uniform grid.

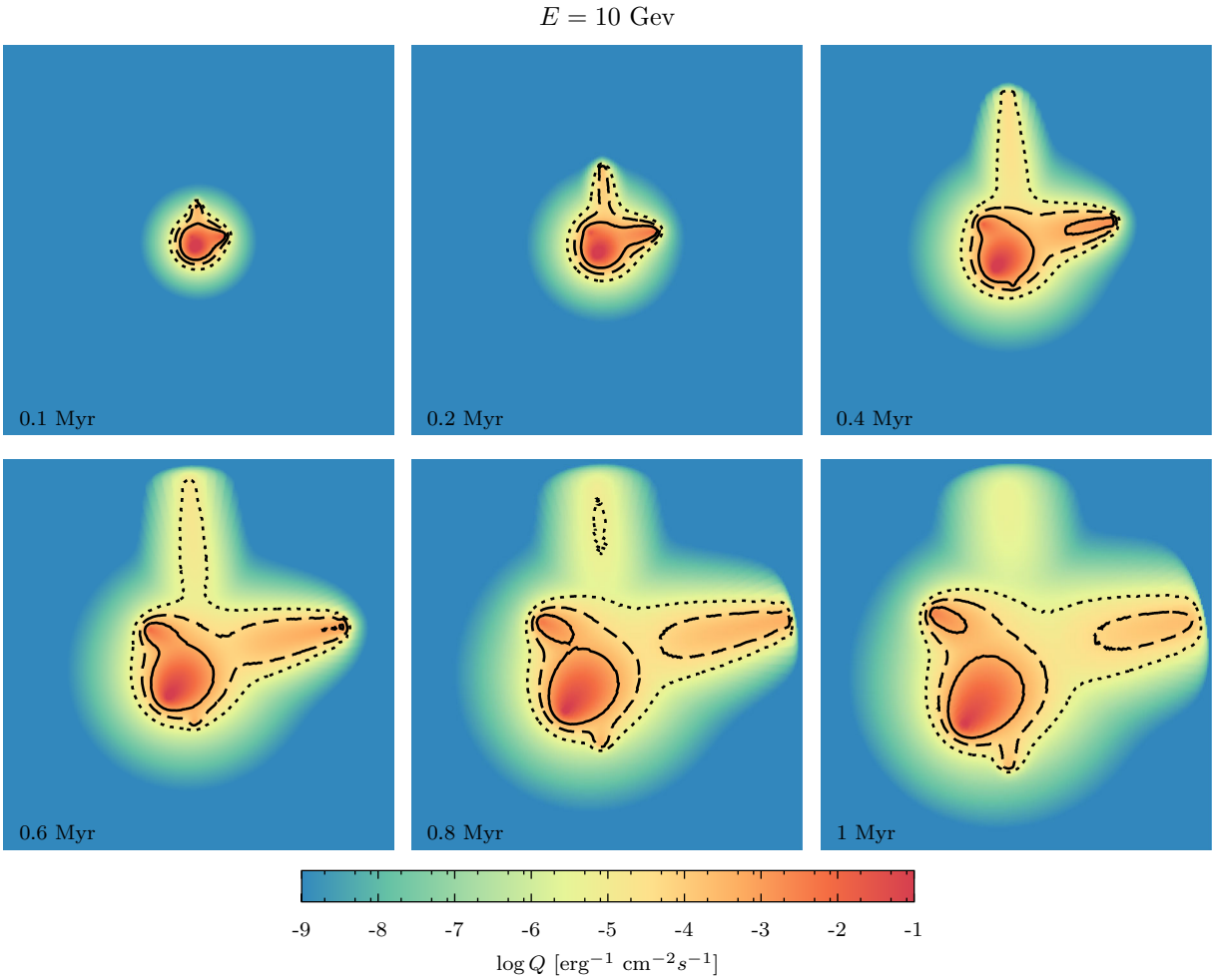

Figure 6. Same as Fig. 5 for slow diffusion ($\chi = 10^{-3}$).

Secondly, we integrate only the diffusion part of the transport equation,

$$\frac{\partial N}{\partial t} = D(E)\left[\frac{1}{R^2}\frac{\partial}{\partial R}\left(R^2\frac{\partial N}{\partial R}\right) + \frac{1}{R^2\sin\theta}\frac{\partial}{\partial\theta}\left(\sin\theta\frac{\partial N}{\partial\theta}\right)\right]. \quad (18)$$

For solving such integration, we use the semi-implicit Cranck–Nicolson method, with the gradients calculated at the cell interfaces, using central differences. This scheme is, therefore, second-order accurate. We then get a second-intermediate solution, $N_{l,i,j}^{n+2/3}$ from the solution $N_{l,i,j}^{n+1/3}$:

$$\frac{N_{l,j,k}^{n+2/3} - N_{l,j,k}^{n+1/3}}{\Delta t} = \frac{1}{2}D(E)\left[L\left(N_{l,i,j}^{n+2/3}\right) + L\left(N_{l,i,j}^{n+1/3}\right)\right], \quad (19)$$

with

$$\begin{aligned} &L(N_{l,j,k}) \\ &= \frac{1}{\Delta V_{i,j}}\left\{\Delta S_{i+1/2,j}\frac{N_{i+1,j} - N_{i,j}}{\Delta R} - \Delta S_{i-1/2,j}\frac{N_{i,j} - N_{i-1,j}}{\Delta R}\right. \\ &\left. + \Delta S_{i,j+1/2}\frac{N_{i,j+1} - N_{i,j}}{R_i\Delta\theta} - \Delta S_{i,j-1/2}\frac{N_{i,j} - N_{i,j-1}}{R_i\Delta\theta}\right\}, \quad (20) \end{aligned}$$

where $\Delta S_{i\pm1/2,\,j}$ and $\Delta S_{i,\,j\pm1/2}$ are the cell surfaces at the interfaces indicated by the indices. Our algorithm first tries to solve the linear system implied by equations (19) and (20) using the iterative Krylov Space scheme GMRESR (Van der Vorst & Vuik 1994); when it fails to converge to the solution (with relative residue $<10^{-7}$ in the 2-norm), it employs our implementation of a Multigrid solver.

Finally, we add the contributions due to the injection using the Euler explicit method:

$$\frac{N_{l,i,j}^{n+1} - N_{l,i,j}^{n+2/3}}{\Delta t} = Q_{l,i,j}^{n+2/3}. \quad (21)$$

Then, the final solution $N_{l,i,j}^{n+1}$ at t^{n+1} is obtained.

The time-steps Δt are chosen in accordance with the Courant–Friedrichs–Lewy stability criterion for the minimum time step of the advection equation ($\delta t_{\rm adv}$, equation 17) and of the diffusion equation ($\delta t_{\rm dif}$, equation 18). We also impose the condition that the time step must be smaller than the time it takes the star to cross one cell ($\delta t_{\rm inj}$). These three time-steps constraints are calculated with the following formulae:

$$\delta t_{\rm adv} = \min\left\{\frac{\Delta E_l}{P(E_l, R_i, \theta_j)}\right\}, \quad (22)$$

$$\delta t_{\rm dif} = \min\left\{\frac{\Delta\theta(\Delta R)^2}{D(E_l)}\right\}, \quad (23)$$

$$\delta t_{\rm inj} = \frac{\Delta R}{V_\star}. \quad (24)$$

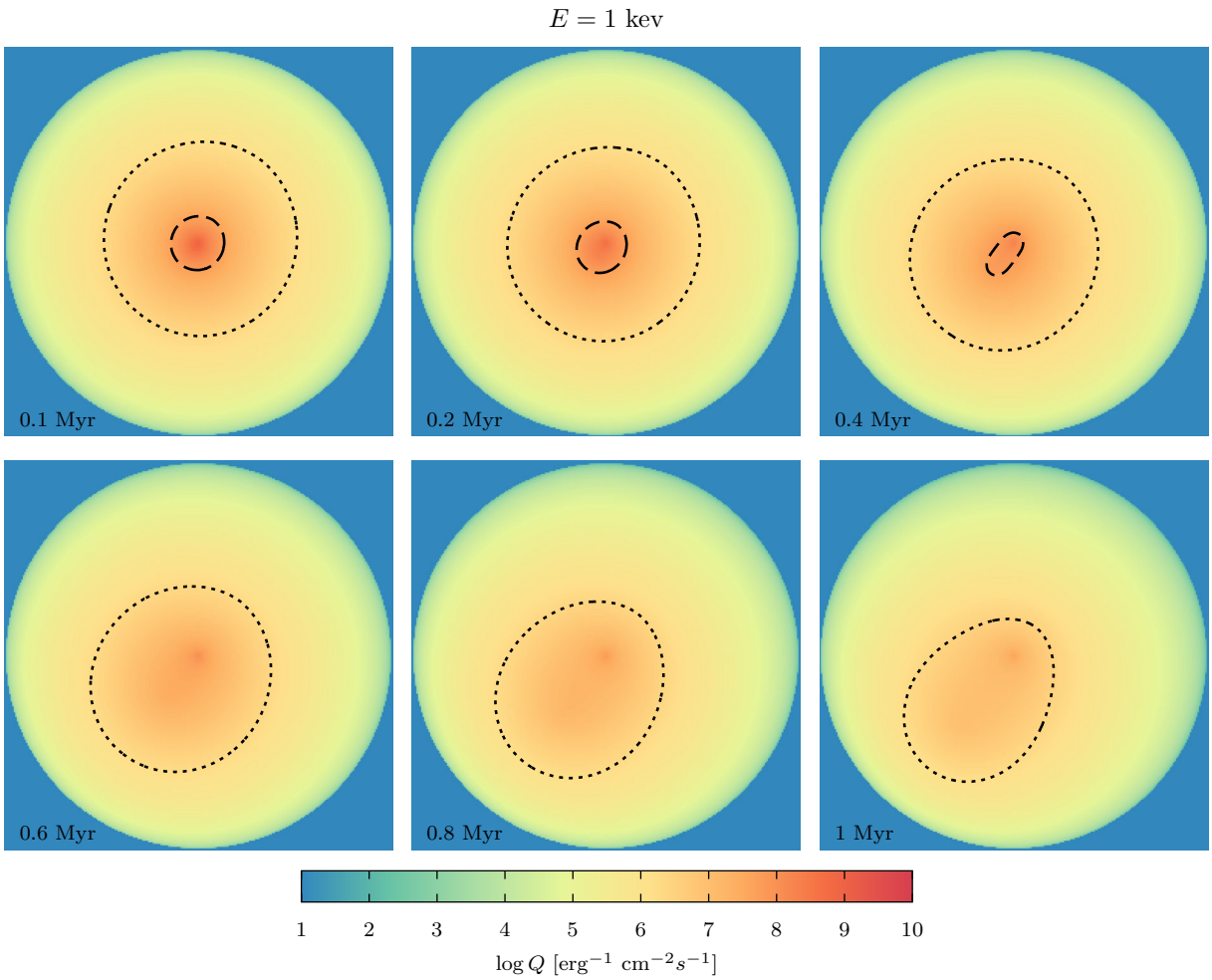

Figure 7. Evolution of the synchrotron emissivity projected along the line of sight, for $\chi = 10^{-1}$. The photon energy is $E = 1$ keV. Time evolves from top left to bottom right. The level curves represent 0.1 (dotted), 1 (dashed), and 10 (continuous) times the background emissivity.

The minimum is taken over all the grid values. The time-step is then $\delta t = \min\{\epsilon_{\rm adv}\delta t_{\rm adv}, \epsilon_{\rm dif}\delta t_{\rm dif}, \epsilon_{\rm inj}\delta t_{\rm inj}\}$. We use the safety factors $\epsilon_{\rm adv} = 0.5$, $\epsilon_{\rm inj} = 0.5$. As the semi-implicit method used for the diffusion equation is unconditionally stable, we use $\epsilon_{\rm dif} = 10$.

We checked the convergence of the solutions presented below performing additional runs (not shown) of some of the models using different resolutions (lower and higher). In addition, we also performed several tests changing the order of the operators sequence (advection, diffusion, injection), and we have not found significant difference between the results.

6 RESULTS

6.1 Particle distributions

In what follows we show series of maps of the protons and $e^{\pm}$ pairs' distributions at a fixed energy and different times, adding the contributions of the six stars. The 2D maps are constructed integrating the 3D data along an arbitrary line of sight, chosen to be on the z direction (see Fig. 1).

In Figs 2 and 3, we show the evolution maps of the proton distribution, for two energies: 10 GeV and 10 TeV, for $\chi = 10^{-1}$ and $\chi = 10^{-3}$, respectively (i.e. fast and slow diffusion). The most energetic particles diffuse faster because of the power-law dependence of $D(E)$ with energy. The different stars can be identified in the maps during the evolution; particularly stars #6 and #4 are seen while they abandon the core region of the cloud. The most energetic star, #1, produces an important anisotropy in the particle distribution.

Fig. 4 shows the evolution maps of the pairs created in the p−p interactions. Maps correspond to two energies: 10 GeV and 1 TeV, for the case $\chi = 10^{-1}$. The pair density is higher in the densest regions of the cloud; in the core also the synchrotron losses are much more intense.

6.2 Emissivity

We calculate the synchrotron emissivity produced by the interaction of the secondary pairs with the inhomogeneous magnetic field given by equation (2). We also compute the emissivity produced in the p−p collisions by neutral pion decays; the target density is $n(R)$, the density of the MC mass, see equation (1). The corresponding formulae can be found in e.g. Aharonian (2004) and references there in. Figs 5 and 6 show the evolution of the gamma emissivity for $E = 10$ GeV, for both diffusion scenarios considered here, respectively. The emission is highly anisotropic and its intensity follows the injectors motion. This is more clear in the case of slow diffusion. The maximum emissivity is reached immediately after the ejection

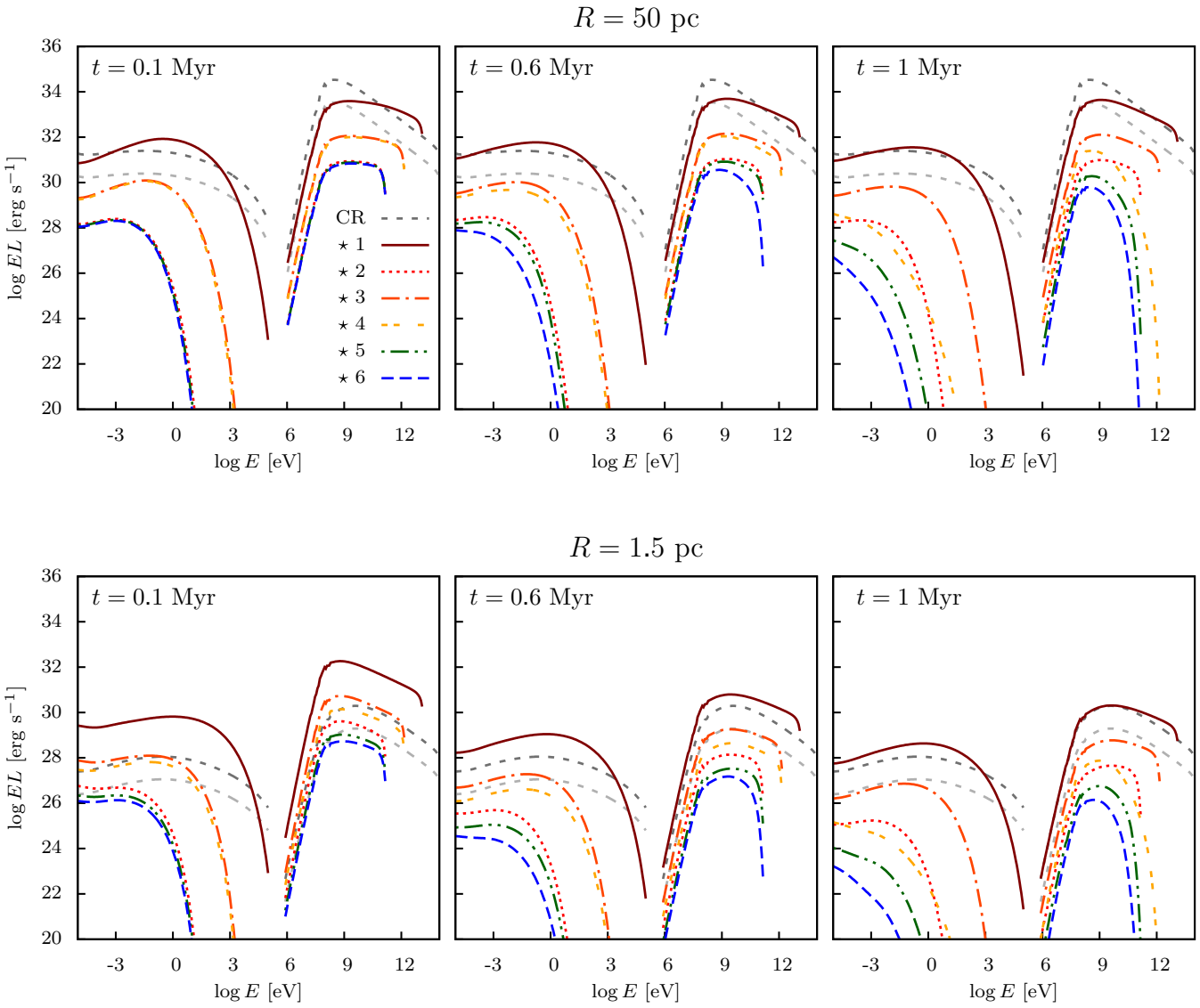

Figure 8. Evolution of the total SED (top) and the nuclear SED (bottom) in the diffusion case $\chi = 10^{-1}$. The emission produced by the CR background is indicated by 'CR'. The light-grey line corresponds to the case in which the flux of CRs is lower than the flux observed locally. Time evolves from left to right.

of the stars, while the high-energy particles are concentrated in the high-density (and high magnetic field intensity) MC core.

Pairs are created with high energies and they produce synchrotron radiation from radio to X-rays. In the maps displayed in Fig. 7, we show the evolution of the synchrotron emissivity projected along the line of sight, for $E = 1$ keV (soft X-rays) and $\chi = 10^{-1}$. Here, we sum the contributions of all stars, but not all of them produce pairs that emit synchrotron radiation up to this energy. Because of the dependence of this emission with the magnetic field ($\propto B^2$), the radiation is considerably more intense in the centre of the cloud, where B is higher.

6.3 Spectral energy distributions

Fig. 8 shows the evolution of the total SEDs – integrated over a sphere of radius $R_{\rm MC} = 50$ pc – and the nuclear SED – integrated inside a sphere of radius $r = 1.5$ pc – for $\chi = 10^{-1}$. The luminosity produced by the CR background is also shown.

The gamma emission and the synchrotron radiation produced by stars #2–#6 are negligible in the total SED, for both CR backgrounds. The contribution of star #1 dominates the spectrum over the luminosity produced by the CRs (dark-grey line in the SEDs) in the energy ranges 10^{-3} eV–1 keV and 100 GeV–10 TeV. If the background of CRs is the lowest case consider here (light-grey line in the SEDs), star #1 dominates the SED in the energy ranges 10^{-5} eV–10 keV and 1 MeV–10 TeV.

In the case of the nuclear SED, the non-thermal emission produced by star #1 dominates over the background emission. The emission from star #3 exceeds the background when the star is near the centre in the energy ranges 10^{-3} eV–10 eV and 1 MeV–1 TeV. If the CR density is lower, the emission produced by the weaker stars (#2, #3, and #4) exceeds the background at radio wavelengths and at energies ∼MeV, when the injection starts. In this case, the contribution of star #3 is greater than the background during a longer time, until ∼0.7 Myr.

Fig. 9 shows the evolutions of the total and nuclear SEDs for the case $\chi = 10^{-3}$ (slow diffusion). In this case, the total SED

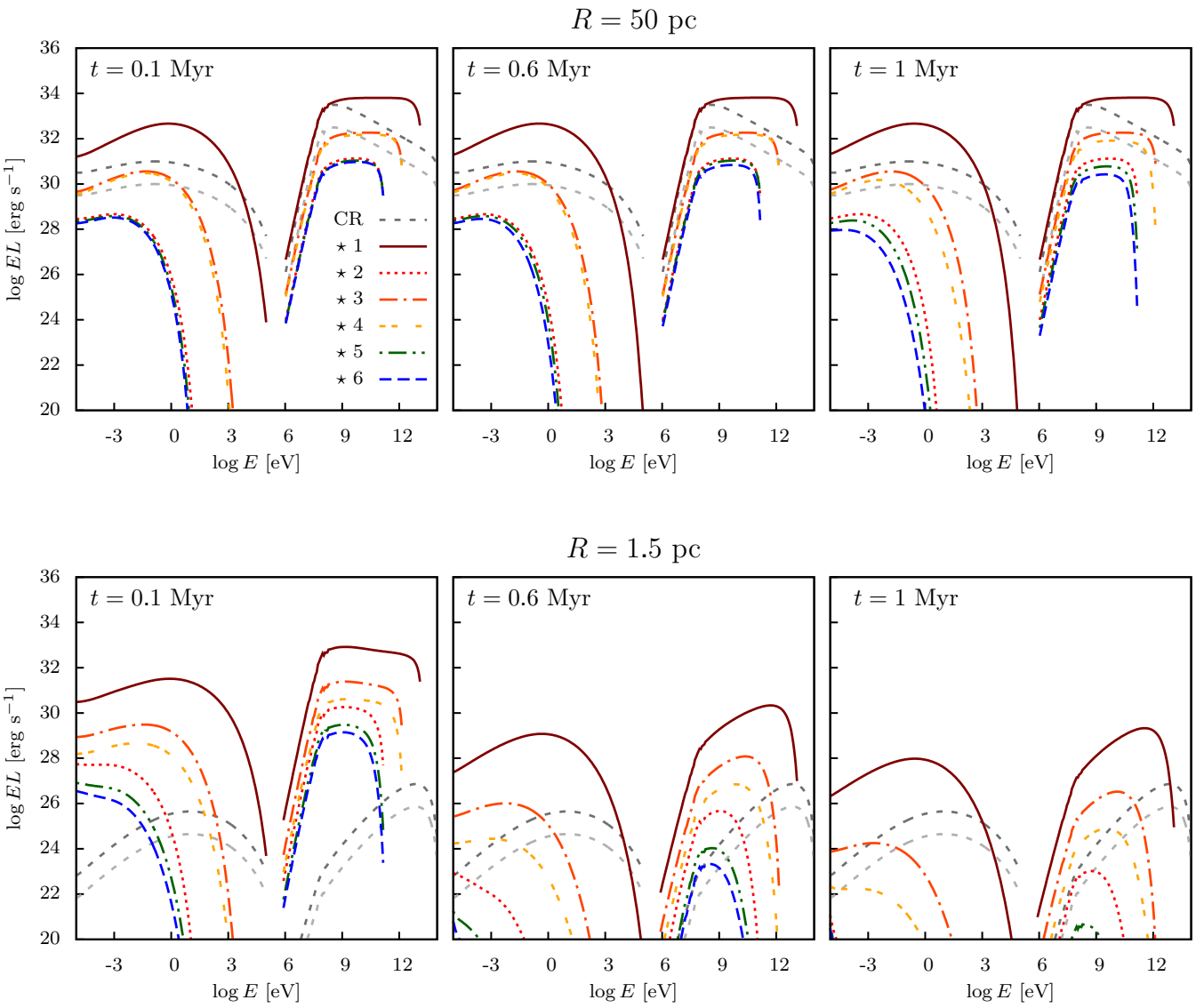

Figure 9. Same as Fig. 8 in the case $\chi = 10^{-3}$.

is dominated by the contribution of star #1, from radio to hard X-rays, and energies from ∼MeV to 10 TeV, during all the integration time. If the level of CRs is the lowest one considered here, stars #3 and #4 also exceed the background during all the integration time from the lowest energies up to 10^2 eV and from 1 MeV to 1 TeV. In the nuclear region, the contribution of all stars exceeds the background (for both values of the CR level considered), when the stars are near the core. Stars #3 and #4 in the range of energies from MeV to GeV and TeV, respectively, overcome the CR contribution even at the final integration time (1 Myr). The slow diffusion makes the injected particles to stay longer inside the cloud, radiating in the denser regions; the CRs penetrate less in the cloud because the larger diffusion time makes the energy losses more efficient.

It should be observed that the electron–positron pairs produced by the background CRs are limited in energy due to our energy grid limit of 10^3 TeV for the CR protons. Changing the upper limit in the energy increases the number of high-energy pairs, and consequently increases the high-energy tail of the background synchrotron emission. However, the increase on the emission is small and occurs at photon energies greater than 1 keV, where the synchrotron emission from the stars decreases.

Finally, the evolution of the total energy in protons (left) and pairs (right) for $\chi = 10^{-1}$ are shown in Fig. 10 (top). The total energy of protons and pairs for stars #1, #2, and #3 increases slowly with time. As the stars move away from the central region of the MC the energy losses diminish as n and B decrease. For stars #4, #5, and #6, the total energy drops with time for $t \gtrsim \tau$ (see Table 1); this is because the injection stops when the star leaves the MC. The evolution of the total gamma (left) and synchrotron (right) luminosity, also for $\chi = 10^{-1}$, can be seen in Fig. 10 (bottom). Initially, the total gamma luminosity increases very fast for all stars. As the stars move away from the centre, n and B decrease. However, the gamma luminosity does not decrease for stars #1, #2, and #3. For the fastest stars (#4, #5, and #6), the gamma luminosity decreases because they leave the MC during the integration time. The total synchrotron luminosity also increases very fast at the beginning, but after some time it starts to decrease for all stars; this might be because B decreases faster than n with R, and due to the quadratic dependence of the synchrotron radiation with B.

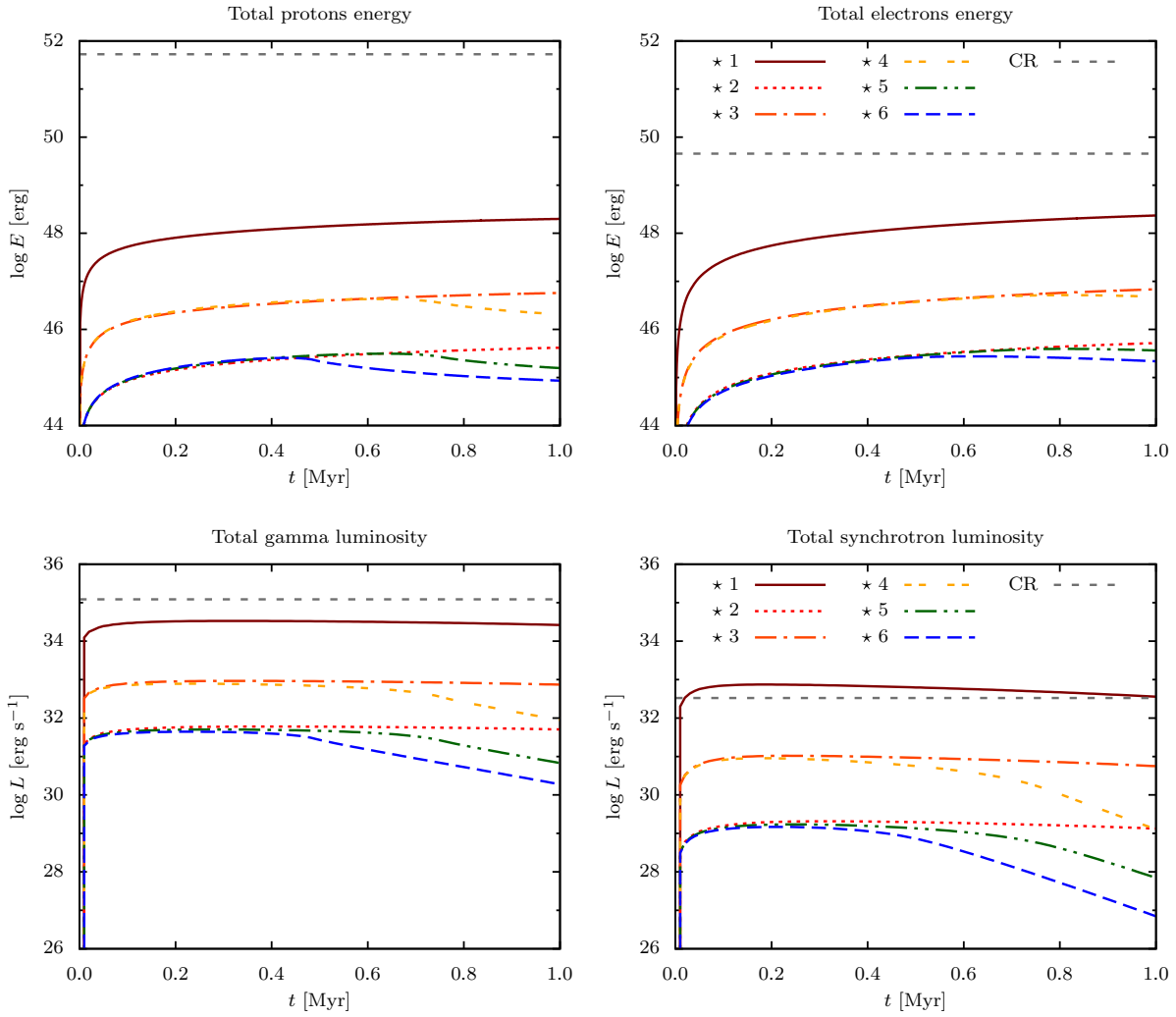

Figure 10. Top: evolution of total energy in protons (left) and pairs (right). Bottom: evolution of the total gamma (left) and synchrotron (right) luminosity. Here $\chi = 10^{-1}$.

7 DISCUSSION AND CONCLUSIONS

The locally injected protons and secondary pairs, under some assumptions, dominate over the CR sea that penetrates the cloud. The gamma-ray luminosity produced by the protons reaches values of the same order as some of the detected luminosities in MCs, e.g. $\sim 10^{34}$ erg s^{-1}.

A very energetic star, as the case of star #1, can inject a significant amount of protons in the medium and it is able to produce important gamma-ray emission over the whole cloud, overcoming the background emission produced by the CR sea. This star dominates the gamma-rays during most of the time in both cases considered here for the diffusion – $\chi = 10^{-1}$ and $\chi = 10^{-3}$. The contribution of the less powerful stars dominates locally over the CR contribution. However, stars with weak winds, as stars #2, #5, and #6 do not inject enough power to overcome globally the emission produced by the CR sea. The injected power we adopt here depends on the acceleration model of particles in bowshocks of runaway stars (del Valle & Romero 2012, 2014), so the actual injected power in specific sources could differ.

The non-thermal emission from radio to X-rays is significant, with luminosities of almost 10^{32} erg s^{-1}. However, in an MC thermal radiation might dominate in many regions of this energy range. Additionally, the absorption produced by the MC matter is expected to be very intense from the IR to soft X-rays. Low radio frequencies are recommended, then, for the observational study of large clouds.

As can be inferred from the cases we present here, the results are very sensitive to particle diffusion and to the ambient CR levels. Both quantities are not very well known. This fact makes the present research particularly valuable in the light of the inverse problem: detailed radio maps, including polarization, along with gamma-ray imaging might become a powerful tool to probe the physical conditions in the clouds.

The hypothesis that a uniform flux of CRs pervades the whole Galaxy can be inappropriate in some cases, especially at small spatial scales (Gabici 2013). The locally observed CR flux might not represent the CR population of the whole Galaxy. The local CR flux as a matter of fact, could be contaminated by a few local sources. This assumption requires an observational confirmation, that might come from gamma-ray observations of nearby passive MCs (Aharonian 2004).

Regarding the diffusion coefficient, additional observations are necessary to obtain solid constraints. The forthcoming gamma-ray observatory CTA might play a fundamental role in this subject

because of its great angular resolution and sensitivity (e.g. Gabici 2013; Pedaletti et al. 2013).

ACKNOWLEDGEMENTS

This work is supported by AYA2010-21782-C03-01 (Spain) and PICT 2007-00848/2012-00878, Préstamo BID (ANPCyT). RSL acknowledges support from the Brazilian agency FAPESP (2013/15115-8). This work has made use of the computing facilities of the Laboratory of Astroinformatics (IAG/USP, NAT/Unicsul), whose purchase was made possible by the Brazilian agency FAPESP (grant 2009/54006-4) and the INCT-A.

REFERENCES

Ackermann M. et al., 2012a, ApJ, 755, 22
Ackermann M. et al., 2012b, ApJ, 756, 4
Actis M. et al., 2011, Exp. Astron., 32, 193
Aharonian F. A., 1991, Ap&SS, 180, 305
Aharonian F. A., 2001, Space Sci. Rev., 99, 187
Aharonian F. A., 2004, Very High Energy Cosmic Gamma Radiation: A Crucial Window on the Extreme Universe. World Scientific, River Edge, NJ
Aharonian F. A., Atoyan A. M., 1996, A&A, 309, 917
Aharonian F. et al., 2005, A&A, 431, 197
Aharonian F. et al., 2006, Nature, 439, 695
Benaglia P., Romero G. E., Martí J., Peri C. S., Araudo A. T., 2010, A&A, 517, L10
Berezinskii V. S., Bulanov S. V., Dogiel V. A., Ptuskin V. S., 1990, Astrophysics of Cosmic Rays. North-Holland, Amsterdam
Bestenlehner J. M. et al., 2011, A&A, 530, L14
Blaauw A., 1961, Bull. Astron. Inst. Neth., 15, 265
Black J. H., Fazio G. G., 1973, ApJ, 185, L7
Bloemen J. B. G. M., Caraveo P. A., Hermsen W., Lebrun F., Maddalena R. J., Strong A. W., Thaddeus P., 1984, A&A, 139, 37
Bodenheimer P. H., 2011, Principles of Star Formation. Springer-Verlag, Berlin
Bosch-Ramon V., Aharonian F. A., Paredes J. M., 2005, A&A, 432, 609
Casse M., Montmerle T., Paul J. A., 1981, in Setti G., Spada G., Wolfendale A. W., eds, Proc. IAU Symp. 94, Cosmic rays from regions of star formation. II - The OB associations. III - The role of T-Tauri stars in the Rho OPH cloud. D. Reidel Publishing Co., Dordrecht, p. 323
Casse F., Lemoine M., Pelletier G., 2002, Phys. Rev. D, 65, 023002
Combi J. A., Romero G. E., 1995, A&A, 303, 872
Combi J. A., Romero G. E., Benaglia P., 1998, A&A, 333, L91
Crutcher R. M., 1999, ApJ, 520, 706
del Valle M. V., Romero G. E., 2012, A&A, 543, A56
del Valle M. V., Romero G. E., 2014, A&A, 563, A96
del Valle M. V., Romero G. E., De Becker M., 2013, A&A, 550, A112
Elitzur M., 1976, ApJ, 203, 124
Fernandez D., Dalton M., Eger P., Laffon H., Mehault J., Ohm S., Oya I., Renaud M., H. E. S. S. Collaboration, 2013, preprint (arXiv:1305.6396)
Fujii M. S., Portegies Zwart S., 2011, Science, 334, 1380
Gabici S., 2011, in Giani S., Leroy C., Rancoita P. G., eds, Cosmic Rays for Particle and Astroparticle Physics. World Scientific, Singapore, p. 343
Gabici S., 2013, in Torres D. F., Reimer O., eds, Astrophysics and Space Science Proc., Vol. 34, Cosmic Rays in Star-Forming Environments. Springer-Verlag, Berlin, p. 221
Gabici S., Aharonian F. A., Blasi P., 2007, Ap&SS, 309, 365
Gies D. R., Bolton C. T., 1986, ApJS, 61, 419
Ginzburg V. L., Syrovatskii S. I., 1964, The Origin of Cosmic Rays. Pergamon, Oxford
Gvaramadze V. V., Kroupa P., Pflamm-Altenburg J., 2010, A&A, 519, A33
Hartmann L., 2009, Accretion Processes in Star Formation, 2nd edn. Cambridge Univ. Press, Cambridge
Hillas A. M., 2005, J. Phys. G: Nucl. Part. Phys., 31, 95
Hoogerwerf R., de Bruijne J. H. J., de Zeeuw P. T., 2000, ApJ, 544, L133
Hunter S. D., Digel S. W., de Geus E. J., Kanbach G., 1994, ApJ, 436, 216
Hunter S. D. et al., 1997, ApJ, 481, 205
Kelner S. R., Aharonian F. A., Bugayov V. V., 2006, Phys. Rev. D, 74, 034018
Kobulnicky H. A., Gilbert I. J., Kiminki D. C., 2010, ApJ, 710, 549
Kraushaar W. L., Clark G. W., Garmire G. P., Borken R., Higbie P., Leong V., Thorsos T., 1972, ApJ, 177, 341
Larson R. B., 2003, Rep. Prog. Phys., 66, 1651
Leonard P. J. T., Duncan M. J., 1988, AJ, 96, 222
López-Santiago J. et al., 2012, ApJ, 757, L6
Malkov M. A., Diamond P. H., Sagdeev R. Z., Aharonian F. A., Moskalenko I. V., 2013, ApJ, 768, 73
Martí J. et al., 2013, A&A, 556, A131
Montmerle T., 1979, ApJ, 231, 95
Nava L., Gabici S., 2013, MNRAS, 429, 1643
Ohm S., Hinton J. A., White R., 2013, MNRAS, 434, 2289
Orellana M., Bordas P., Bosch-Ramon V., Romero G. E., Paredes J. M., 2007, A&A, 476, 9
Ormes J. F., Ozel M. E., Morris D. J., 1988, ApJ, 334, 722
Pedaletti G., Torres D. F., Gabici S., de Oña Wilhelmi E., Mazin D., Stamatescu V., 2013, A&A, 550, A123
Perets H. B., Šubr L., 2012, ApJ, 751, 133
Peri C. S., Benaglia P., Brookes D. P., Stevens I. R., Isequilla N. L., 2012, A&A, 538, A108
Ptuskin V. S., Zirakashvili V. N., Plesser A. A., 2008, Adv. Space Res., 42, 486
Reimer O., Aharonian F., Hinton J., Hofmann W., Hoppe S., Raue M., Reimer A., 2008, in Hamann W.-R., Feldmeier A., Oskinova L. M., eds, Clumping in Hot-Star Winds. Universität Potsdam, Potsdam, p. 195
Santos-Lima R., Lazarian A., de Gouveia Dal Pino E. M., Cho J., 2010, ApJ, 714, 442
Simpson J. A., 1983, Annu. Rev. Nucl. Part. Sci., 33, 323
Torres D. F., Dame T. M., Digel S. W., 2005, ApJ, 621, L29
van Buren D., McCray R., 1988, ApJ, 329, L93
Van der Vorst H. A., Vuik C., 1994, Numer. Linear Algebra Appl., 1, 369
Voelk H. J., Forman M., 1982, ApJ, 253, 188
Yan H., Lazarian A., 2004, ApJ, 614, 757
Yan H., Lazarian A., 2008, ApJ, 673, 942
Yan H., Lazarian A., 2011, ApJ, 731, 35
Yan H., Lazarian A., Schlickeiser R., 2012, ApJ, 745, 140

This paper has been typeset from a TEX/LATEX file prepared by the author.